J. Fluid Mech. (2020), *vol*. 900, A13. © The Author(s), 2020.
Published by Cambridge University Press
doi:10.1017/jfm.2020.496

Optimal perturbations in viscous round jets subject to Kelvin–Helmholtz instability

Gabriele Nastro[1],†, **Jérôme Fontane**[1] **and Laurent Joly**[1]

[1]ISAE-SUPAERO, Université de Toulouse, 31055 Toulouse, France

(Received 5 November 2019; revised 8 April 2020; accepted 11 June 2020)

We investigate the development of three-dimensional instabilities on a time-dependent round jet undergoing the axisymmetric Kelvin–Helmholtz (KH) instability. A non-modal linear stability analysis of the resulting unsteady roll-up into a vortex ring is performed based on a direct-adjoint approach. Varying the azimuthal wavenumber m, the Reynolds number Re and the aspect ratio α of the jet base flow, we explore the potential for secondary energy growth beyond the initial phase when the base flow is still quasi-parallel and universal shear-induced transient growth occurs. For $Re = 1000$ and $\alpha = 10$, the helical $m = 1$ and double-helix $m = 2$ perturbations stand as global optimals with larger growth rates in the post roll-up phase. The secondary energy growth stems from the development of elliptical (E-type) and hyperbolic (H-type) instabilities. For $m > 2$, the maximum of the kinetic energy of the optimal perturbation moves from the large scale vortex core towards the thin vorticity braid. With a Reynolds number one order of magnitude larger, the kinetic energy of the optimal perturbations exhibits sustained growth well after the saturation time of the base flow KH wave and the underlying length scale selection favours higher azimuthal wavenumbers associated with H-type instability in the less diffused vorticity braid. Doubling the jet aspect ratio yields initially thinner shear layers only slightly affected by axisymmetry. The resulting unsteady base flow loses scale selectivity and is prone to a common path of initial transient growth followed by the optimal secondary growth of a wide range of wavenumbers. Increasing both the aspect ratio and the Reynolds number thus yields an even larger secondary growth and a lower wavenumber selectivity. At a lower aspect ratio of $\alpha = 5$, the base flow is smooth and a genuine round jet affected by the axisymmetry condition. The axisymmetric modal perturbation of the base flow parallel jet only weakly affects the first common phase of transient growth and the optimal helical perturbation $m = 1$ dominates with energy gains considerably larger than those of larger azimuthal wavenumbers whatever the horizon time.

Key words: Jets

1. Introduction

Understanding the mechanisms by which initially laminar flows transition to turbulence is of fundamental importance in fluid dynamics, especially in the context of mixing promotion. Due to its occurrence in many industrial applications aiming at mixing an

† Email address for correspondence: gabriele.nastro@isae-supaero.fr

effluent with a background fluid, round jet is a prototypical flow to which many authors have devoted special attention in the past. The main features of round jet transition have been widely studied allowing for a characterisation of its initial phase, which is ruled by the development of corotating vortex rings resulting from the primary Kelvin–Helmholtz (KH) instability of the axisymmetric shear layer (Becker & Massaro 1968). This inviscid primary instability is a prototypical inflectional instability (Drazin & Reid 1981) whose streamwise and azimuthal wavenumbers can be determined through a classical local linear stability analysis (Batchelor & Gill 1962; Lessen & Singh 1973; Crighton & Gaster 1976; Morris 1976; Plaschko 1979; Michalke 1984). The azimuthal wavenumber m is necessarily an integer and defines the azimuthal periodicity of the instability: axisymmetric perturbations correspond to $m = 0$; helical ones to $m = 1$; double-helix ones to $m = 2$ and so on. The selection of the most unstable mode depends on both the Reynolds number Re and the steepness of the base flow velocity profile, measured by the aspect ratio $\alpha = \ell_0/\vartheta$ where ℓ_0 is the jet radius and ϑ is the shear layer momentum thickness (Jimenez-Gonzalez, Brancher & Martinez-Bazan 2015). Fully developed jet velocity profiles corresponding to low aspect ratios α, i.e. profiles with a thick vorticity layer, are generally unstable to helical perturbations ($m = 1$) whatever the Reynolds number, as shown by Batchelor & Gill (1962) in their pioneering work. Conversely, steeper so-called top-hat jet profiles, characterised by large values of α, present a wider range of unstable azimuthal wavenumbers (Michalke 1964; Plaschko 1979), including axisymmetric disturbances ($m = 0$) which become the most unstable for vanishing shear layer thickness in the inviscid limit (Abid, Huerre & Brachet 1993). However, perturbations with higher azimuthal wavenumbers $m \geq 2$ are always less unstable than the axisymmetric or helical ones. A similar response has been retrieved for low aspect ratios and top-hat jets when considering low-Reynolds-number jets, although the viscosity plays a stabilising role that yields lower growth rates (Lessen & Singh 1973; Morris 1976). Therefore, the most unstable primary mode of the round jet undergoes a transition from helical to axisymmetric azimuthal periodicity when the velocity profile steepness increases (Jimenez-Gonzalez *et al.* 2015).

The vortex ring resulting from the nonlinear evolution of the primary KH instability experiences two kinds of secondary instabilities. The first one is the two-dimensional subharmonic pairing of two consecutive billows which induces an increase of their size combined with a doubling of the streamwise wavelength (Yule 1978; Reynolds & Bouchard 1981). When promoted or spontaneously occurring, the subharmonic pairing has been demonstrated to merely delay the onset of the second type of secondary instabilities (Moser & Rogers 1993; Rogers & Moser 1993; Arratia, Caulfield & Chomaz 2013). These are three-dimensional and lead to the development of streamwise counter-rotating vortices along the 'braid', i.e. along the stretched axisymmetric vorticity sheet connecting two consecutive primary structures. These longitudinal 'rib' vortices wrap around the KH vortex rings and cause an azimuthal deformation of their cores, as observed experimentally by Yule (1978), Liepmann (1991) and Liepmann & Gharib (1992). No global stability analysis has been conducted so far to determine the three-dimensional secondary modes of the round jet associated with these three-dimensional structures. However, their development has been analysed numerically by Martin & Meiburg (1991) and Brancher, Chomaz & Huerre (1994) by introducing an arbitrary azimuthal deformation of the initial velocity profile. They found the same physical mechanism described by Lasheras, Cho & Maxworthy (1986) and Lasheras & Choi (1988) to be responsible in the plane mixing layer for the development of the rib vortices in the braid region. This strong similarity with the three-dimensionalisation of the plane mixing layer allows one to transpose the

results of the stability analyses conducted in that case (Pierrehumbert & Widnall 1982; Klaassen & Peltier 1991; Caulfield & Kerswell 2000; Fontane & Joly 2008; Arratia *et al.* 2013, amongst others) to the jet flow. The three-dimensionalisation of the flow results from the combined development of two secondary modes: a small wavenumber core-centred elliptical (E-type) instability, originally coined by Pierrehumbert & Widnall (1982) as the 'translative' instability due to the induced spanwise periodic displacement of the vortex core, and a large wavenumber braid-centred hyperbolic (H-type) instability; following Arratia *et al.* (2013).

The present work intends to perform a global stability analysis over the whole unsteady evolution from the initially parallel jet flow to the roll-up of the KH vortex rings in order to determine the secondary instabilities of the round jet and to analyse which specific features come from the axisymmetry of the base flow compared with the plane mixing layer. Adopting the temporal approach, we discard any non-parallel effects such as the frequency and wavenumber drifts downstream an otherwise spatially developing flow. We also filter out the effect of two-dimensional subharmonic pairing by restricting the time-dependent base flow to a streamwise extent equivalent to the wavelength of the most unstable KH mode. We compensate for the phase velocity of the most unstable KH mode to follow the base flow unsteady roll-up in a reference frame moving with the primary mode, at least initially. Due to the unsteadiness of the base flow and the non-normality of the governing equations, the classical modal approach, which predicts the asymptotic long-time exponential behaviour of perturbations, is not suited for capturing the short time unstable dynamics and to account for the influence of the base flow temporal evolution on the secondary modes (Schmid 2007). Therefore, we opt for a non-modal analysis based on a direct-adjoint approach, similar to the one conducted by Arratia *et al.* (2013) and Lopez-Zazueta, Fontane & Joly (2016) for the plane shear layer, and look for the optimal perturbation growing over temporally evolving KH vortex rings.

In the case of the plane shear layer, Arratia *et al.* (2013) found that both E-type and H-type instabilities initially grow thanks to a combination of the Orr (1907) and lift-up (Ellingsen & Palm 1975; Landahl 1975, 1980) mechanisms. The Orr mechanism is purely two-dimensional and relies on the deformation of vorticity patches under the action of the base flow shear. The deformation induces a transient energy growth due to the temporary concentration of vorticity, which, owing to the Kelvin circulation preservation theorem, increases vorticity extrema of vorticity patches initially aligned with the direction of compression, as illustrated in figure 1(*a*). The lift-up mechanism, originally identified in wall-bounded shear flows, is associated with pairs of counter-rotating streamwise vortices which lift fluid of low momentum in high velocity regions and reciprocally move high momentum fluid towards lower velocity regions, generating streamwise aligned layers of streamwise velocity perturbations, or so-called streamwise velocity streaks, as shown in figure 1(*b*). Arratia *et al.* (2013) also observed that the E-type mode is the global optimal when perturbation is injected from the initial development of the flow while the H-type becomes dominant only when the optimisation interval starts after the initial period of transient growth. Thus, the selection of an E-type or an H-type perturbation depends on both the spanwise wavenumber and the injection time of the initial perturbation. The outcome of these optimal perturbations leads in both cases to the formation of streamwise counter-rotating vortices in the braid region.

In the case of the round jet, a non-modal stability analysis has already been conducted, but only for the primary instability. Garnaud *et al.* (2013*a*) have found that the largest transient energy gains are due to helical perturbations, leading the authors to suggest that a lift-up mechanism could be involved. Boronin, Healey & Sazhin (2013) came to

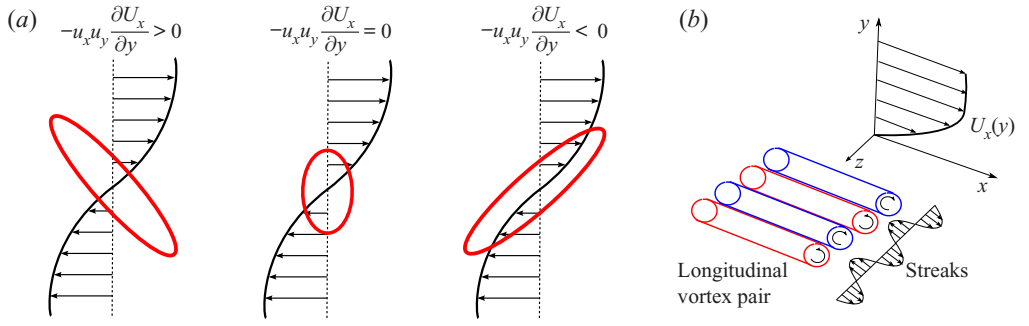

FIGURE 1. Sketches of (*a*) Orr and (*b*) lift-up transient growth mechanisms. For the Orr mechanism, the term $-u_x u_y(\partial U_x/\partial y)$ on the figure indicates the source term active in the equation of the perturbation kinetic energy.

a similar conjecture based on the amplification of the streamwise velocity component of the perturbation. Conversely, the results of Garnaud *et al.* (2013*b*) on the optimal forcing of the jet suggest the contribution of an Orr-type mechanism to the perturbation's growth. The recent studies of Jimenez-Gonzalez *et al.* (2015) and Jimenez-Gonzalez & Brancher (2017) on both the steady and the unsteady diffusing base flow identified the existence of three distinct mechanisms depending on both the axial and azimuthal wavenumbers of the perturbation. For axisymmetric perturbations, the transient growth relies on the Orr mechanism with the reorientation of initial azimuthal vorticity structures under the action of the base flow shear. This mechanism is observed to be more efficient at large axial wavenumber when the Reynolds number is increased. In the helical case, the Orr mechanism is also responsible for the transient growth of the perturbation at large wavenumbers. However, for small axial wavenumbers, the energy of the perturbation mostly lies in the streamwise vorticity component and induces a radial displacement of the jet as a whole. This 'shift-up' mechanism is thus very specific to the $m = 1$ perturbation at low wavenumber. Indeed, for higher values of the azimuthal wavenumber, i.e. $m \geq 2$, the structure of the optimal perturbation is more concentrated along the shear layer and is associated with the classical lift-up mechanism. The transient energy growth of the perturbation is always found to be more efficient in the helical case whatever the Reynolds number and the aspect ratio of the base flow. The present work also aims at ascertaining whether these transient mechanisms are active in the development of secondary instabilities of the round jet.

The paper is organised as follows. The governing equations and the numerical methods are presented in § 2 together with a description of the base flow. The results of the non-modal stability analysis for the nonlinear KH vortex rings are discussed in § 3. The influence of the azimuthal wavenumber m, the optimisation interval (both the injection t_0 and horizon T times), the Reynolds number Re and the aspect ratio α of the initial velocity profile on the optimal perturbation is considered. Finally, conclusions and perspectives are drawn in § 4.

2. Formulation of the problem

2.1. *Base flow*

We consider an incompressible fluid flow in a cylindrical reference frame (r, θ, z) with the r, θ and z axes corresponding to the radial, azimuthal and streamwise directions,

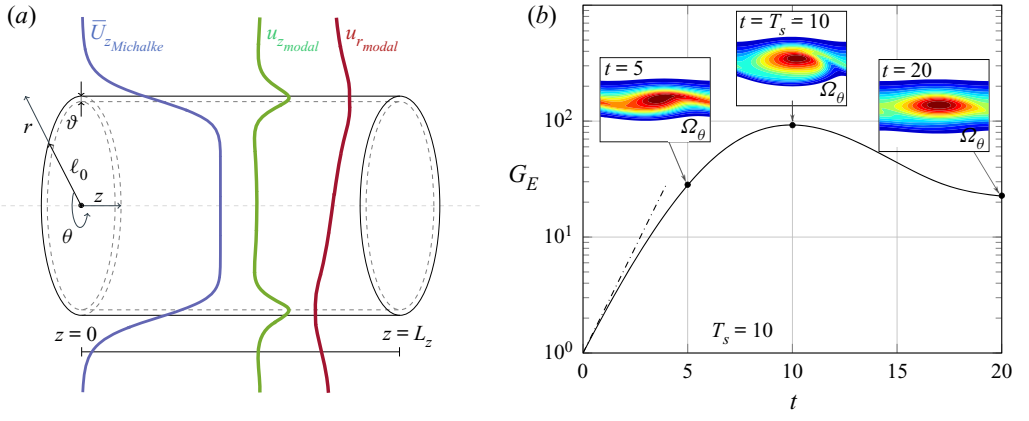

FIGURE 2. (*a*) Definition of the cylindrical reference frame together with a sketch of the initial condition of the simulation of the base flow. Here, the initial amplitude of the KH mode has been rescaled for sake of clarity. (*b*) Temporal evolution of the energy gain G_E of the KH mode for $\alpha = 10$. The insets represent the azimuthal vorticity of the base flow Ω_θ shown at times $t = 5$, $t = T_s = 10$ and $t = 20$. The dash-dotted line stands for the energy growth predicted by the linear stability analysis.

respectively, as illustrated in figure 2(*a*). We denote ℓ_0 and u_0 the characteristic length and velocity scales taken as the jet radius and the jet centreline velocity at the nozzle exit, respectively. As we address buoyancy-free flows, the dimensionless Navier–Stokes equations read

$$\boldsymbol{\nabla} \cdot \boldsymbol{u} = 0, \tag{2.1}$$

$$D_t \boldsymbol{u} = -\boldsymbol{\nabla} p + \frac{1}{Re} \boldsymbol{\Delta} \boldsymbol{u}, \tag{2.2}$$

where $D_t = \partial_t + (\boldsymbol{u} \cdot \boldsymbol{\nabla})$ denotes the material derivative and $Re = (\rho_0 u_0 \ell_0)/\mu$ is the Reynolds number with μ the dynamic viscosity and $\rho_0 = 1$ the constant density. Following the works of Arratia *et al.* (2013), Jimenez-Gonzalez *et al.* (2015), Lopez-Zazueta *et al.* (2016) and Jimenez-Gonzalez & Brancher (2017), we will set the Reynolds number $Re = 1000$ (except in § 3.2, where we deal with the effect of variations in Re), which is large enough to guarantee that the primary KH mode wraps itself into a finite amplitude, energetic vortex ring.

The two-dimensional base flow consists of a time-evolving axisymmetric jet which undergoes the nonlinear development of the primary KH instability starting from the classical profile proposed by Michalke (1971). The corresponding velocity $\boldsymbol{U} = [U_r, 0, U_z]$ and pressure fields P are computed on a meridian plane of dimension $[-r_{max}, r_{max}] \times [0, L_z]$ through a direct numerical simulation using a two-dimensional dealiased pseudo-spectral method described in detail in Joly, Fontane & Chassaing (2005) and Joly & Reinaud (2007). In particular, we adopt a Fourier expansion in the streamwise direction and a Chebyshev collocation method for the radial direction (Khorrami, Malik & Ash 1989). The Gauss–Lobatto collocation points defined in the Chebyshev space ($\mathcal{R} \in [-1, 1]$) are mapped into the physical space ($r \in [-r_{max}, r_{max}]$) thanks to a logarithmic mapping given by

$$r = a \tanh^{-1}(b\mathcal{R}) \quad \text{with } b = \tanh\left(\frac{r_{max}}{a}\right), \tag{2.3}$$

α	ℓ_0	c	r_{max}	$100\,a_{KH}$	L_z/ℓ_0	T_s
5	1.27	0.757	8.89	1.77	4.95	20.0
6	1.51	0.718	10.6	1.91	4.15	16.7
7	1.74	0.688	12.2	1.94	3.60	14.3
8	1.97	0.665	13.8	1.95	3.19	12.5
9	2.18	0.647	15.7	1.91	2.88	11.1
10	2.39	0.633	16.7	1.88	2.63	10.0
12.5	2.92	0.606	20.4	1.76	2.15	8.00
15	3.45	0.588	24.2	1.64	1.82	6.67
17.5	3.98	0.575	27.9	1.55	1.56	5.71
20	4.52	0.566	31.6	1.49	1.39	5.00

TABLE 1. Main numerical parameters for the simulated homogeneous KH base flow fields: aspect ratio α; jet radius ℓ_0; phase velocity of KH mode c; maximum radius r_{max}; initial amplitude of the KH mode a_{KH}; and ratio L_z/ℓ_0 between the domain streamwise extent and the jet radius and KH saturation time T_s.

where the parameter a controls the stretching of the collocation points. A free-slip boundary condition is imposed at the radial boundaries ($r = \pm r_{max}$) of the flow domain, while the flow is periodic in the streamwise direction.

As illustrated in figure 2(a), the initial condition used for the simulation of the base flow is the profile of Michalke (1971) $\overline{U} = [0, 0, \overline{U}_z]$ given by

$$\overline{U}_z(r) = \frac{1}{2} + \frac{1}{2}\tanh\left[\frac{\alpha}{4}\left(\frac{1}{r} - r\right)\right], \tag{2.4}$$

where $\alpha = \ell_0/\vartheta$ is the jet aspect ratio with ϑ the shear layer momentum thickness, perturbed by the most unstable mode obtained by the inviscid temporal linear stability analysis. The temporal modal analysis yields the phase velocity $c(\alpha)$ of the dispersion relation of the most unstable mode. We compensate for this phase velocity over the whole velocity field to keep the KH vortex ring at the centre of the Galilean reference frame. The saturation time T_s of the primary instability depends on the initial amplitude of the KH mode a_{KH}, the Reynolds number Re and the aspect ratio α. The initial amplitude a_{KH}, defined as the square root of the ratio between the initial kinetic energy of the KH mode and the Michalke profile, is chosen small enough to ensure the existence of a linear phase of growth and its value is set so that the linear phase is the same for all cases, i.e. $\alpha T_s = 100$. The jet radius ℓ_0 is set so that the most amplified KH mode corresponds to a wavenumber of $2\pi/L_z$. The radial extent of the domain is chosen large enough to ensure that the free-slip boundary condition has no influence on the nonlinear development of the flow, i.e. $r_{max} = 7\ell_0$. For all simulations, we use a mesh of 512^2 points, which has been checked to be large enough to ensure the convergence of the results. All the numerical settings for the homogeneous KH base flow fields are summarised in table 1.

Figure 2(b) shows the temporal evolution of the energy gain $G_E = E(t)/E(t_0)$ of the primary KH instability for $\alpha = 10$. During the initial phase, the energy grows exponentially in time at a rate consistent with the growth rate predicted by the linear stability analysis. The nonlinear saturation of the mode occurs at $T_s = 10$ and results in the unsteady roll-up of the axisymmetric shear layer into a KH vortex ring as illustrated by the contours of the azimuthal vorticity Ω_θ in the insets of figure 2(b). In contrast with

the plane shear layer case, the KH vortex does not exhibit a central symmetry with respect to the elliptical stagnation point, which is specific to the axisymmetry condition.

2.2. *Optimisation problem*

We now consider the temporal linear evolution of three-dimensional disturbances $[\boldsymbol{u}, p]$ that are likely to grow over the incompressible KH vortex ring $[\boldsymbol{U}, P]$. The governing equations (2.1) and (2.2) are linearised around the two-dimensional base flow:

$$\boldsymbol{\nabla} \cdot \boldsymbol{u} = 0, \tag{2.5}$$

$$\frac{\partial \boldsymbol{u}}{\partial t} + \boldsymbol{U} \cdot \boldsymbol{\nabla} \boldsymbol{u} + \boldsymbol{u} \cdot \boldsymbol{\nabla} \boldsymbol{U} = -\boldsymbol{\nabla} p + \frac{1}{Re} \boldsymbol{\Delta} \boldsymbol{u}. \tag{2.6}$$

We can write this linear system – referred to as the direct system – in the following compact form:

$$\boldsymbol{N}_t \cdot \boldsymbol{q} + \boldsymbol{N}_c \cdot \boldsymbol{q} + \frac{1}{Re} \boldsymbol{N}_d \cdot \boldsymbol{q} = 0, \tag{2.7}$$

where $\boldsymbol{q} = [\boldsymbol{u}, p]$ is the direct variable vector and the three matrix operators are the temporal operator $\boldsymbol{N}_t$, the operator of coupling between the base flow and the disturbance $\boldsymbol{N}_c$ and the operator of viscous diffusion $\boldsymbol{N}_d$, respectively.

The base flow being time-dependent and the dynamical system (2.7) non-normal, we resort to a non-modal stability analysis for which the temporal behaviour of the perturbation is not prescribed. Taking into account the streamwise periodicity and the axisymmetry of the base flow, the perturbation can be written in the form

$$[u_r, u_\theta, u_z, p](r, \theta, z, t) = \frac{1}{2} \left([\tilde{u}_r, \tilde{u}_\theta, \tilde{u}_z, \tilde{p}](r, z, t)\, \mathrm{e}^{\mathrm{i}(\mu z + m\theta)} + \text{c.c.} \right), \tag{2.8}$$

where m is the azimuthal wavenumber and $\mu \in [0,\ 1]$ the real Floquet exponent. As advocated in the introduction, the case where the base flow exhibits two-dimensional pairing is not considered here. Moreover, the works of Klaassen & Peltier (1991) and Fontane & Joly (2008) showed that the unstable modes of the stratified and the inhomogeneous mixing layers are only weakly sensitive to the Floquet exponent. For these reasons, we look for perturbations having the same streamwise periodicity as the base flow, i.e. $\mu = 0$.

Amongst all possible perturbations likely to develop within the KH vortex ring, we are interested in those maximising the growth of kinetic energy over a finite time interval $[t_0, T]$. The energy gain G_E is defined as the ratio between the perturbation kinetic energy at the horizon time T and the one at the injection time t_0:

$$G_E(T, t_0) = \frac{E(T)}{E(t_0)} = \frac{\|\boldsymbol{q}(T)\|_u}{\|\boldsymbol{q}(t_0)\|_u}, \tag{2.9}$$

where $\|\cdot\|_u$ stands for the seminorm associated with the conventional inner product and the kinetic energy (see appendix A for definition). In accordance with the pioneering work of Farrell (1988), we define the optimal perturbation as the one reaching the maximal energy gain

$$\mathcal{G}_E(T, t_0) = \max_{\boldsymbol{q}(t_0)} \{G_E(T, t_0)\}, \tag{2.10}$$

over all the possible initial conditions $\boldsymbol{q}(t_0)$. To determine this optimal perturbation, we solve an optimisation problem with constraints (Gunzburger 2002) enforcing the

disturbance to be a solution of the linearised Navier–Stokes equations (2.5) and (2.6). It can be converted to an optimisation problem without constraints by using the variational method of the Lagrange multipliers (see Luchini & Bottaro 1998; Corbett & Bottaro 2000, 2001). This approach involves the derivation of the so-called adjoint equations (Schmid 2007) associated with the direct system (2.5) and (2.6):

$$\boldsymbol{\nabla}\cdot\boldsymbol{u}^{\dagger}=0, \tag{2.11}$$

$$-\frac{\partial \boldsymbol{u}^{\dagger}}{\partial t}-\boldsymbol{U}\cdot\boldsymbol{\nabla}\boldsymbol{u}^{\dagger}+\boldsymbol{u}^{\dagger}\cdot\boldsymbol{\nabla}\boldsymbol{U}^{\mathrm{T}}=\boldsymbol{\nabla}p^{\dagger}+\frac{1}{Re}\boldsymbol{\Delta}\boldsymbol{u}^{\dagger}, \tag{2.12}$$

where $\boldsymbol{u}^{\dagger}$ denotes the adjoint variable of the velocity field, $p^{\dagger}$ is the adjoint pressure and the superscript $^{\mathrm{T}}$ stands for the matrix transpose. The adjoint system can be also cast in the following compact form:

$$-\boldsymbol{N}_t\cdot\boldsymbol{q}^{\dagger}+\boldsymbol{N}_c^{\dagger}\cdot\boldsymbol{q}^{\dagger}+\frac{1}{Re}\boldsymbol{N}_d\cdot\boldsymbol{q}^{\dagger}=0, \tag{2.13}$$

where $\boldsymbol{q}^{\dagger}=[\boldsymbol{u}^{\dagger},\,p^{\dagger}]$ is the adjoint variable vector. The negative sign before the temporal operator $\boldsymbol{N}_t$ implies a backward-in-time integration of the adjoint equations. Here, $\boldsymbol{N}_c^{\dagger}$ represents the adjoint coupling matrix operator between the base flow and the adjoint disturbance.

The identification of the optimal perturbation and the associated optimal energy gain $\mathcal{G}_E$, relies on an iterative optimisation algorithm described in detail in appendix A. The direct system (2.7) is advanced in time until the horizon time T, from an initial condition $\boldsymbol{q}(t_0)$ taken as a white noise. From the final direct state obtained at T, we compute the initial condition $\boldsymbol{q}^{\dagger}(T)$ for the adjoint system (2.13), before its integration backward-in-time to the injection time t_0. The resulting state is rescaled and used for the subsequent direct-adjoint integration. The optimisation loop is stopped when a 0.5 % convergence is achieved on the kinetic energy gain (see (A 5)). When compared with a perturbation obtained with a 0.1 % convergence rate, the L_2-norm of the difference between velocity fields remains below 2 % in relative value. Both direct and adjoint systems are integrated with the linearised version of the two-dimensional dealiased pseudo-spectral method used for the generation of the base flow. A rapid convergence of the optimisation problem is obtained in fewer than ten iterations.

We resort to the evolution equation for the energy growth rate of the perturbation $\sigma_E=(1/E)\,\mathrm{d}E/\mathrm{d}t$ to analyse the physical mechanisms associated with the energy growth of the optimal perturbations. This equation can be derived straightforwardly from the transport equation of the perturbation kinetic energy $E=\|\boldsymbol{q}\|_u$:

$$\begin{aligned}\frac{\mathrm{d}E}{\mathrm{d}t}=&\underbrace{-\int_{\mathcal{V}}u_ru_z\left(\frac{\partial U_r}{\partial z}+\frac{\partial U_z}{\partial r}\right)\mathrm{d}\mathcal{V}}_{\Pi_{E_1}}\underbrace{-\int_{\mathcal{V}}\left(u_r^2\frac{\partial U_r}{\partial r}+u_\theta^2\frac{U_r}{r}+u_z^2\frac{\partial U_z}{\partial z}\right)\mathrm{d}\mathcal{V}}_{\Pi_{E_2}}\\&\underbrace{-\frac{1}{Re}\int_{\mathcal{V}}(\boldsymbol{\nabla}\boldsymbol{u}:\boldsymbol{\nabla}\boldsymbol{u}^{T})\,\mathrm{d}\mathcal{V}}_{\Pi_{E_\Phi}},\end{aligned} \tag{2.14}$$

where the symbol **:** stands for the double contracted tensor product, Π_{E_1} is the energy production/destruction due to the base flow shear, Π_{E_2} the energy production/destruction due to the base flow strain field and Π_{E_Φ} the viscous dissipation of energy.

3. Optimal perturbations of a round jet

3.1. *Optimal energy growth*

We first consider the optimal perturbations of a round jet characterised by an aspect ratio $\alpha = 10$ when injected at the initial time of the development of the base flow, i.e. $t_0 = 0$. Figure 3 displays the temporal evolution of the energy gain $\mathcal{G}_E$ of perturbations optimised for four horizon times between half the saturation time T_s of the base flow KH wave and twice T_s, and for azimuthal wavenumbers ranging from $m = 0$ to $m = 5$. The time normalisation by T_s will be used throughout the paper. The evolution of the energy gain of optimal perturbations growing over a diffusing unperturbed parallel jet with the Michalke profile, as obtained by Jimenez-Gonzalez *et al.* (2015), has been added for comparison. For the diffusing parallel jet, the energy curves are all superimposed indicating that increasing the horizon time does not modify the path but only raises the final energy gain reached by the disturbance. Therefore, the computation of the optimal perturbation for the largest horizon time explored is sufficient to access the energy gain evolution for any smaller T. The presentation of the optimal perturbations growing on a diffusing Michalke profile will be limited to that sole case in the following. Up to $t \sim T_s/2$, all perturbations follow the same energy growth while the still quasi-parallel base flow is in the linear phase of the KH instability. Even when optimised for long time horizons, the optimal perturbations thus exhibit the same primary growth as the one developing over a parallel jet. The influence of the nonlinear roll-up in the base flow is felt after $t \sim T_s/2$, corresponding to the onset of roll-up and of azimuthal vorticity concentration in the base flow, as illustrated in figure 2(*b*). This is the turning point where perturbations optimised for horizon times beyond the saturation time evolve from a primary to a secondary type. The onset of the nonlinear roll-up in the base flow yields the energy decrease of the axisymmetric optimal perturbation and bounds the energy growth of the helical and doubly helical ones. Conversely, for larger azimuthal wavenumbers, i.e. $m > 2$, optimal perturbations developing over a diffusive parallel jet experience a substantial drop of energy, while perturbations optimised over a nonlinear KH roll-up benefit from a secondary phase of renewed though moderate energy growth.

Figure 4(*a*) displays the final energy gain at horizon time $\mathcal{G}_E$ as a function of the horizon time T extended to $3T_s$, for the same values of the azimuthal wavenumber. The optimal energy gain of perturbations growing over a diffusing Michalke profile has also been included in the background for reference. Whatever the azimuthal wavenumber, the energy gain grows on a similar trend until $T \approx 0.5T_s$ up to a value of $\mathcal{G}_E \approx 10^2$. For all m, most of the perturbation energy growth is produced during this first phase. This initial period corresponds to the linear phase of the primary KH instability during which the axisymmetric shear layer has not rolled-up yet. After this initial phase, the energy of the axisymmetric disturbance $m = 0$ continues to increase up to a maximal value obtained for a horizon time equal to the saturation time $T = T_s$ before decreasing monotonically when T is increased further. The energy of the non-axisymmetric perturbations keeps on growing, although not always monotonically, when the horizon time is increased beyond $T \approx 0.5T_s$. In particular, the helical mode is the only one to exhibit a monotonic energy growth. It stands as the so-called global optimal, the one displaying the largest energy growth over all wavenumbers up to $T \approx 2.5T_s$, when it is overtaken by the $m = 2$ mode. If we consider $[T_s, 2T_s]$ as the most favourable period for the development of secondary instabilities in real jets, the overall maximum energy gain corresponds to a helical perturbation whatever the horizon time, at least for the present values of the aspect ratio α and Reynolds number Re.

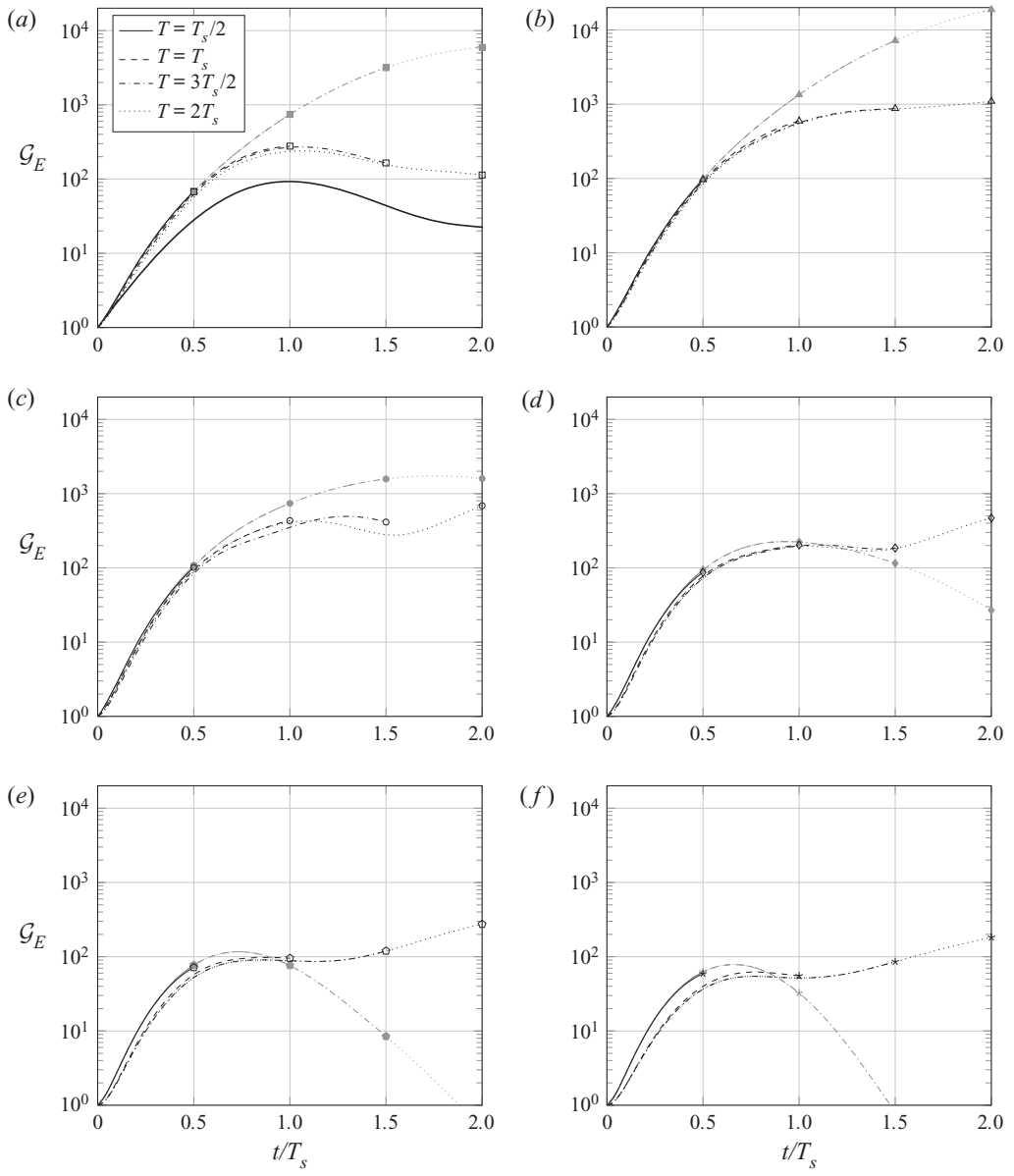

FIGURE 3. Temporal evolution of the energy gain $\mathcal{G}_E$ for optimal perturbations growing over the roll-up of a nonlinear KH wave (black lines) and for the ones developing over a diffusing Michalke profile (grey lines) for six azimuthal wavenumbers: (*a*) $m = 0$; (*b*) $m = 1$; (*c*) $m = 2$; (*d*) $m = 3$; (*e*) $m = 4$; and (*f*) $m = 5$. The thick continuous line in panel (*a*) represents the temporal evolution of the energy gain of the primary KH mode, as displayed in figure 2(*b*). The symbols are located at the horizon time of each energy curve.

In order to compare the growth efficiency of the various perturbations over the optimisation time frame, we consider the mean optimal energy growth rate σ_m defined as follows:

$$\sigma_m = \frac{1}{T/T_s}\int_0^{T/T_s} \sigma_E(t)\,\mathrm{d}t = \frac{\ln\left[\mathcal{G}_E(T/T_s)\right]}{T/T_s}. \tag{3.1}$$

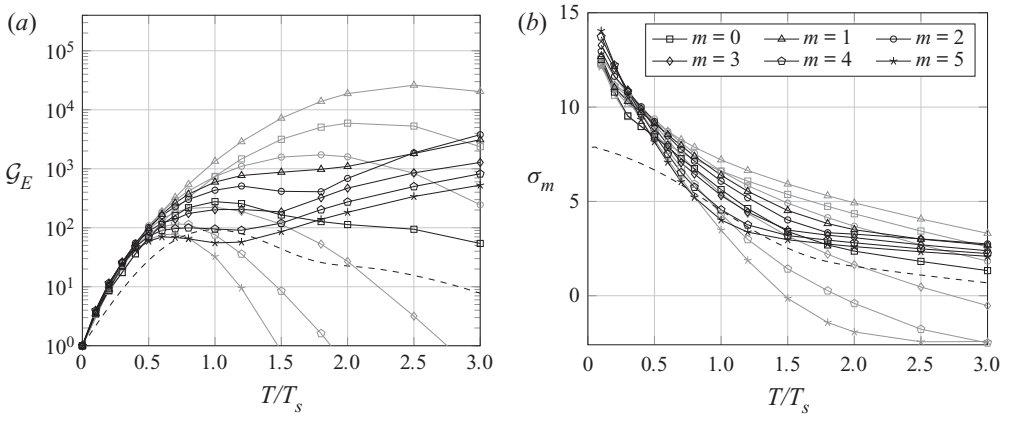

FIGURE 4. (*a*) Optimal energy gain $\mathcal{G}_E$ as a function of the normalised horizon time T/T_s for different azimuthal wavenumbers at an injection time of $t_0 = 0$. (*b*) Influence of the azimuthal periodicity m on the mean optimal growth rate σ_m as a function of T/T_s. Dashed black lines correspond to the temporal evolution of (*a*) the energy gain G_E and (*b*) the mean growth rate of the primary KH mode. Grey lines represent the optimal energy gain of perturbations growing over a diffusing Michalke profile.

Figure 4(*b*) presents the evolution of σ_m with the time ratio T/T_s for all the azimuthal wavenumbers considered here. As T increases, σ_m decreases monotonically confirming that most of the energy growth occurs in the early times of the base flow evolution, i.e. before the nonlinear saturation of the KH wave into a roll-up. For the shortest horizon time considered here, $T = 0.1T_s$, one can see that σ_m increases monotonically with the azimuthal wavenumber m (the largest is obtained for $m = 5$), but immediately after (for $T \geq 0.2T_s$) the hierarchy changes and the helical mode progressively emerges as the global optimal until $T \approx 2.5T_s$ when it is overtaken by the double-helix perturbation ($m = 2$) in accordance with the optimal energy gain $\mathcal{G}_E$ in figure 4(*a*).

We now focus on the spatial distribution of the energy during the time evolution in the interval $[0, T_s]$ of perturbations optimised for $T = T_s$, as displayed in figure 5.

At $t = t_0$, the optimal perturbations take the form of two elongated oblique layers whatever the azimuthal wavenumber m. These structures characterised by different azimuthal periodicity according to m value are orientated along the direction of maximal compression of the base flow. During the time interval $[t_0, T_s/2]$, as the jet shear layer gradually rolls up into a vortex ring, these layers are progressively deformed under the action of the base flow mean shear in such way so as to be reoriented along the direction of base flow maximal stretching. This short-times evolution reflects the combination of Orr (1907) and lift-up (Ellingsen & Palm 1975) mechanisms, identified to be responsible for the transient energy growth of so-called 'OL' perturbations in plane shear layers (Arratia *et al.* 2013; Lopez-Zazueta *et al.* 2016). The subsequent evolution of the axisymmetric $m = 0$ perturbation for $t \geq T_s/2$ leads to a perturbation dipole located between the vortex core and the braid of the KH vortex ring. Once the shear-induced deformation has brought the initial energy growth due to the Orr-mechanism, the perturbation energy dipole is slowly dissipated but does not benefit from any three-dimensional relay mechanism for a secondary energy growth. For non-axisymmetric perturbations, the energy perturbation at the horizon time $T = T_s$ evolves progressively from a core-centred to a braid-centred distribution when m is increased, as indicated by the location of the energy maximum

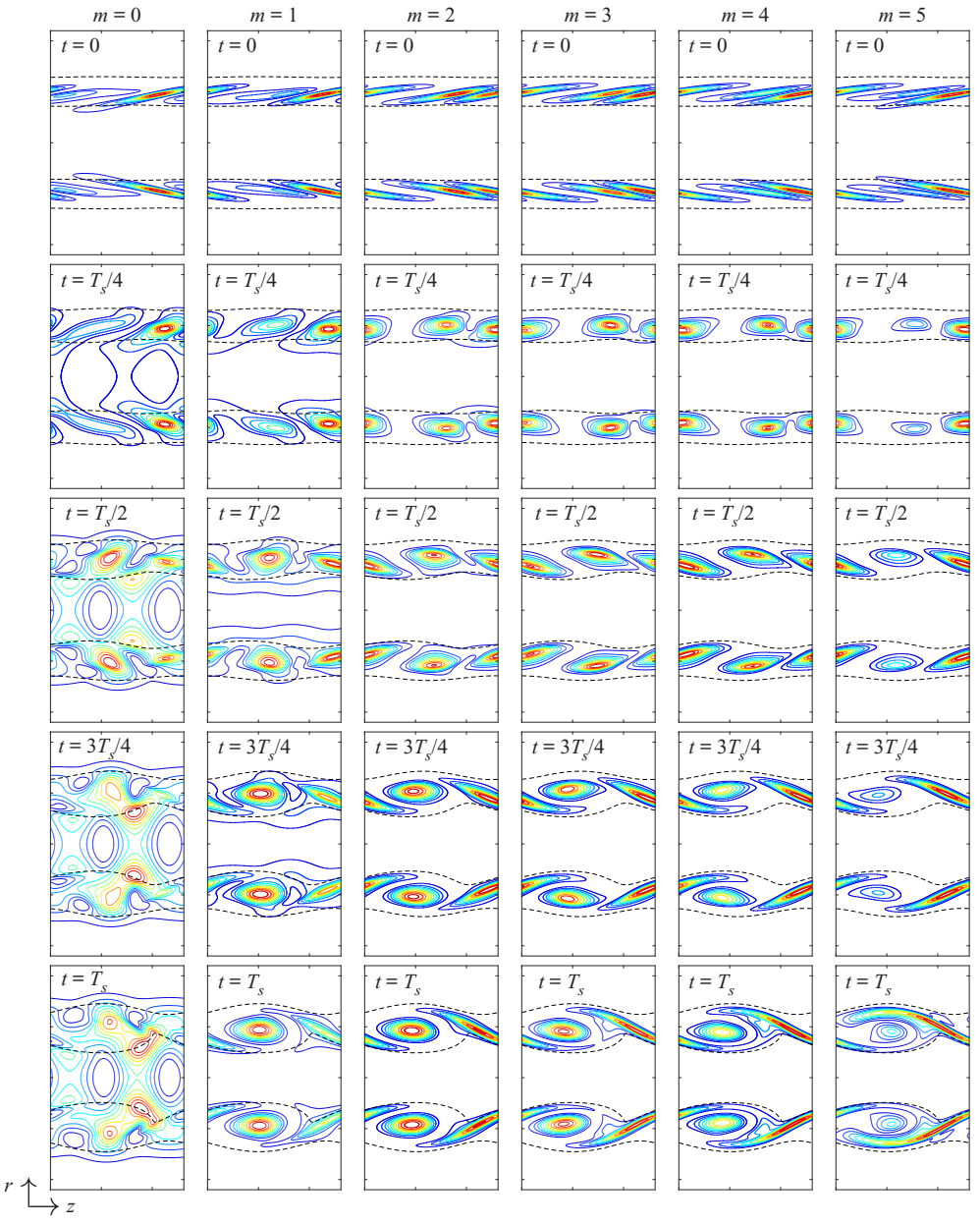

FIGURE 5. Temporal evolution of the field of kinetic energy E of optimal perturbations from $t = t_0$ to $t = T_s$ for various azimuthal wavenumbers. The energy is normalised by its current time maximum value and ten equally spaced coloured contour levels are used. Tick marks along the r and z axes correspond to the jet radius ℓ_0. Dashed contours correspond to 20 % of the maximal absolute value of the base flow azimuthal vorticity Ω_θ.

in figure 5. At low m, the perturbation lies preferentially in the KH vortex core where the streamlines are locally elliptical and corresponds to an E-type instability while, at high m, the perturbation induces oscillations in the braid region where the streamlines are locally hyperbolic suggesting an H-type instability. This is analogous to the mixing layer

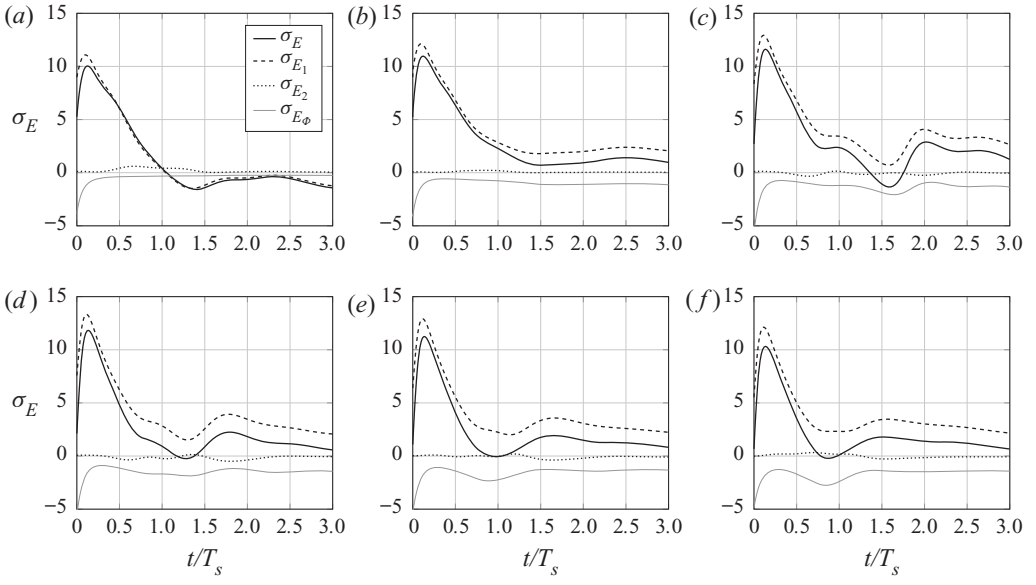

FIGURE 6. Temporal evolution of the kinetic energy growth rate σ_E and its different contributions according to (2.14) for the optimal perturbation with a horizon time $T = 1.5T_s$ and various azimuthal wavenumbers: (*a*) $m = 0$; (*b*) $m = 1$; (*c*) $m = 2$; (*d*) $m = 3$; (*e*) $m = 4$; and (*f*) $m = 5$.

(Arratia *et al.* 2013) and the parallel wake (Ortiz & Chomaz 2011) where the secondary instabilities develop, respectively, on two-dimensional KH billows and on the von Kármán vortex street. Indeed higher azimuthal wavenumbers are associated with shorter azimuthal wavelengths and their associated perturbations are expected to grow in regions of the base flow where length scales are smaller. The hyperbolic region where the vorticity braid thickness decreases in time due to stretching thus naturally hosts the energy growth of large azimuthal wavenumber perturbations. Nevertheless, this scale selection between E-type and H-type perturbations with respect to m is not exclusive since all the cases illustrated in figure 5 display energy in both regions, at least for the present values of azimuthal wavenumber m, aspect ratio α and Reynolds number Re.

The large amplification at short times, as seen in figure 4, is a typical feature of shear flows (Ortiz & Chomaz 2011; Arratia *et al.* 2013; Garnaud *et al.* 2013*a*; Jimenez-Gonzalez *et al.* 2015; Lopez-Zazueta *et al.* 2016; Jimenez-Gonzalez & Brancher 2017). The energy growth during this initial period is essentially due to base flow shear conversion as can be seen in figure 6 which presents the contributions to the temporal evolution of the energy growth rate according to (2.14) for perturbations optimised at $T = 1.5T_s$ from $m = 0$ to $m = 5$. As shown in figure 4(*b*) for the mean optimal growth rate, the energy growth is most efficient in the early times of the base flow evolution, i.e. $t \leq T_s$. The contribution of the base flow strain (term σ_{E_2}) remains very weak and the energy growth results essentially from the net balance between the base flow shear conversion σ_{E_1} and the viscous dissipation σ_{E_Φ}. This is very similar to the results of Arratia *et al.* (2013) for the E-type instability (see their figure 7*a*) whose growth relies on both Orr and lift-up mechanisms. As detailed in the introduction, the Orr mechanism is a two-dimensional mechanism associated with changes in the area of the support of azimuthal vorticity patches under the action of the base flow mean shear. Given the constraint due to the

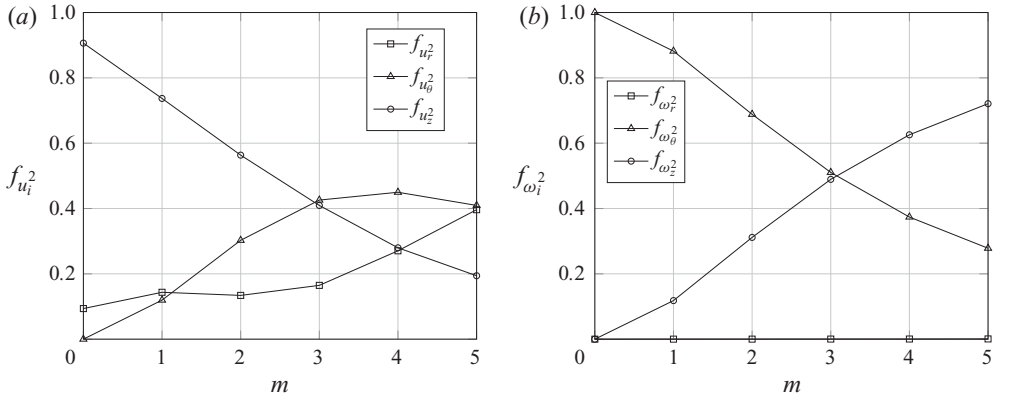

FIGURE 7. Initial contribution to (*a*) the energy of each velocity component $f_{u_i^2}$ and (*b*) the enstrophy of each vorticity component $f_{\omega_i^2}$, as a function of the azimuthal wavenumber m. The horizon time is $T = 1.5T_s$.

Kelvin theorem that the circulation remains constant in the inviscid limit, any reduction in the support area increases azimuthal vorticity. It stems from a pure azimuthal perturbation vorticity ω_θ and induces the amplification of both radial velocity u_r and axial velocity u_z. On the other hand, the lift-up mechanism corresponds to the emergence of streaks of high and low streamwise velocity under the action of the base flow mean shear onto an initial perturbation made of an array of counter-rotating streamwise vortices. It is associated with an initial perturbation of axial vorticity ω_z which leads to large production of axial velocity streaks u_z. As explained by Farrell & Ioannou (1993), the growth of the optimal perturbations in shear flows generally results from a synergistic combination of these two mechanisms: the radial perturbation velocity, fed by the Orr mechanism, enhances the streamwise rolls associated with streak production of the lift-up mechanism. The present case is no exception and the steep increase in energy in the early development of the perturbations observed in figure 6 is also due to this synergy. In this regard, we measure the relative contribution of each mechanism to the energy growth of the perturbation through the following ratios between the contribution of each component of velocity (vorticity) to the perturbation kinetic energy (enstrophy) at the injection time t_0:

$$f_{u_i^2} = \frac{\displaystyle\int_{\mathcal{V}} u_i^2(t_0)\,\mathrm{d}\mathcal{V}}{E(t_0)}, \quad f_{\omega_i^2} = \frac{\displaystyle\int_{\mathcal{V}} \omega_i^2(t_0)\,\mathrm{d}\mathcal{V}}{Z(t_0)}, \tag{3.2a,b}$$

where the subscript i stands for the ith coordinate of the reference frame. Figure 7 shows these ratios as a function of the azimuthal wavenumber m.

In the axisymmetric case, only the radial and axial velocity components have non-zero value. The optimal perturbation thus takes advantage of a pure Orr mechanism ($f_{\omega_\theta^2} = 1$ and $f_{\omega_r^2} = f_{\omega_z^2} = 0$). When the azimuthal wavenumber is increased, the contribution of the azimuthal velocity becomes more significant (so does the radial velocity) and the optimal perturbation gradually organises itself to benefit from both mechanisms. Figure 7(*b*) shows that the two mechanisms contribute equally for $m = 3$ ($f_{\omega_\theta^2} \sim f_{\omega_z^2}$) and then the lift-up becomes more efficient than the Orr mechanism for $m > 3$ ($f_{\omega_\theta^2} < f_{\omega_z^2}$). Therefore, the combination of these two mechanisms ranges from a pure Orr-based growth for $m = 0$ (lift-up is not active in two dimensions) to a predominance of lift-up for $m = 5$.

As already observed by Arratia *et al.* (2013) and Lopez-Zazueta *et al.* (2016) in the homogeneous free shear layer, postponing the injection time t_0 does not change the physics but only reduces the efficiency of Orr and lift-up mechanisms, since the initial period during which these transient growth mechanisms are active is shorter. This is also the case here for the round jet.

3.2. *Influence of the Reynolds number Re*

In this section we investigate the influence of the Reynolds number Re on the transient energy growth of secondary three-dimensional perturbations. Figure 8 displays the temporal evolution of the energy gain $\mathcal{G}_E$ for optimal perturbations obtained at $Re = 10\,000$ compared with those calculated at $Re = 1000$ for various horizon times and azimuthal wavenumber m. Increasing the Reynolds number results in a substantial increase of the energy gains for all perturbations. This is explained by two combined effects. First, the base flow exhibits sharper velocity gradients associated with higher levels of shear and the resulting energy production due to the base flow shear, i.e. term σ_{E_1} in (2.14), is stronger. Second, the viscous dissipation σ_{E_Φ} is lowered with the increase of the Reynolds number.

The temporal evolution from $t = t_0$ to the horizon time T, corresponding to the base flow saturation time T_s, of the spatial distribution of optimal perturbations kinetic energy is illustrated in figure 9 for azimuthal wavenumbers up to $m = 5$. The optimal perturbations at initial time are very similar to those obtained for $Re = 1000$, albeit the inclined layers are thinner. Their evolution during the time interval $[t_0, T_s/2]$, i.e. during linear phase of the KH mode growth in the base flow, results from shear induced deformation and the associated energy growth due to Orr and lift-up mechanisms. At horizon time, the energy is unevenly distributed between the core and the braid region of the KH vortex ring. With increasing azimuthal wavenumber, the transition from an E-type instability to an H-type instability is observed earlier versus the $Re = 1000$ case. For $m \geq 2$, the energy growth lies preferentially in the braid region and the occurrence of an E-type response is even absent for $m \geq 5$. The increase in Reynolds number yields a thinner braid promoting the growth of perturbations with higher azimuthal wavenumbers. The scale selection underlying the outcome of E-type and H-type instabilities with optimal energy growth is steeper for larger Reynolds numbers.

We analyse the structure of the initial perturbation by measuring the relative contribution $f_{u_i^2}$ of velocity components to the energy and $f_{\omega_i^2}$ of vorticity components to the enstrophy in the optimal perturbation at $t = t_0$ according to (3.2). Figure 10 displays the evolution of the structure of the initial perturbation with growing azimuthal wavenumber at $Re = 10\,000$ together with those obtained for $Re = 1000$. In the two-dimensional axisymmetric case, the optimal perturbation only takes advantage of the Orr mechanism, and, as m increases, the Orr mechanism remains predominant over the lift-up mechanism, since $f_{\omega_\theta^2} > f_{\omega_z^2}$, at least up to $m = 5$. Finally, increasing the Reynolds number results in larger energy gains and the promotion of higher azimuthal wavenumbers with no change in the nature of the underlying physical mechanisms.

3.3. *Round jet and free shear layer behaviours*

Finally, we analyse the influence of the aspect ratio α on the optimal energy gain in order to study the effect of steepness of the initial jet velocity profile on the transient growth of secondary instabilities.

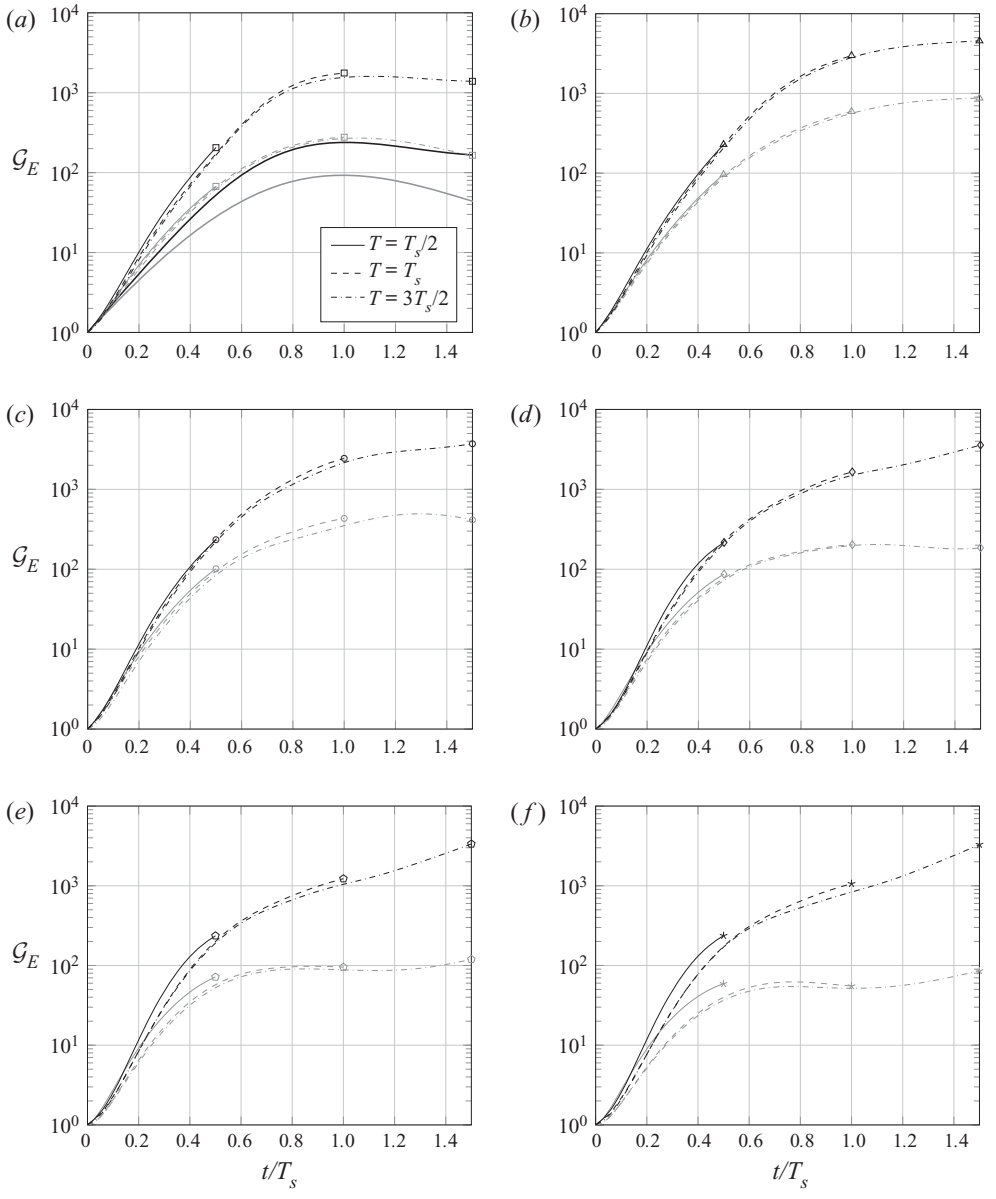

FIGURE 8. Temporal evolution of the energy gain $\mathcal{G}_E$ of optimal perturbations at $Re = 10\,000$ (black lines) and $Re = 1000$ (grey lines) for various azimuthal wavenumbers: (*a*) $m = 0$; (*b*) $m = 1$; (*c*) $m = 2$; (*d*) $m = 3$; (*e*) $m = 4$; and (*f*) $m = 5$. The thick continuous lines in panel (*a*) represent the temporal evolution of the energy gain G_E of the KH mode for the two cases. The symbols denote the optimisation time of each curve.

We first consider the optimal perturbations developing in a round jet characterised by an aspect ratio of $\alpha = 20$. In this case the shear layer momentum thickness is twice smaller than before compared with the jet radius, so that the cylindrical geometry does not have much effect on the flow development, which results to be comparable to a plane free shear layer. Figure 11(*a*) displays the final energy gain at horizon time $\mathcal{G}_E$ as a function of the

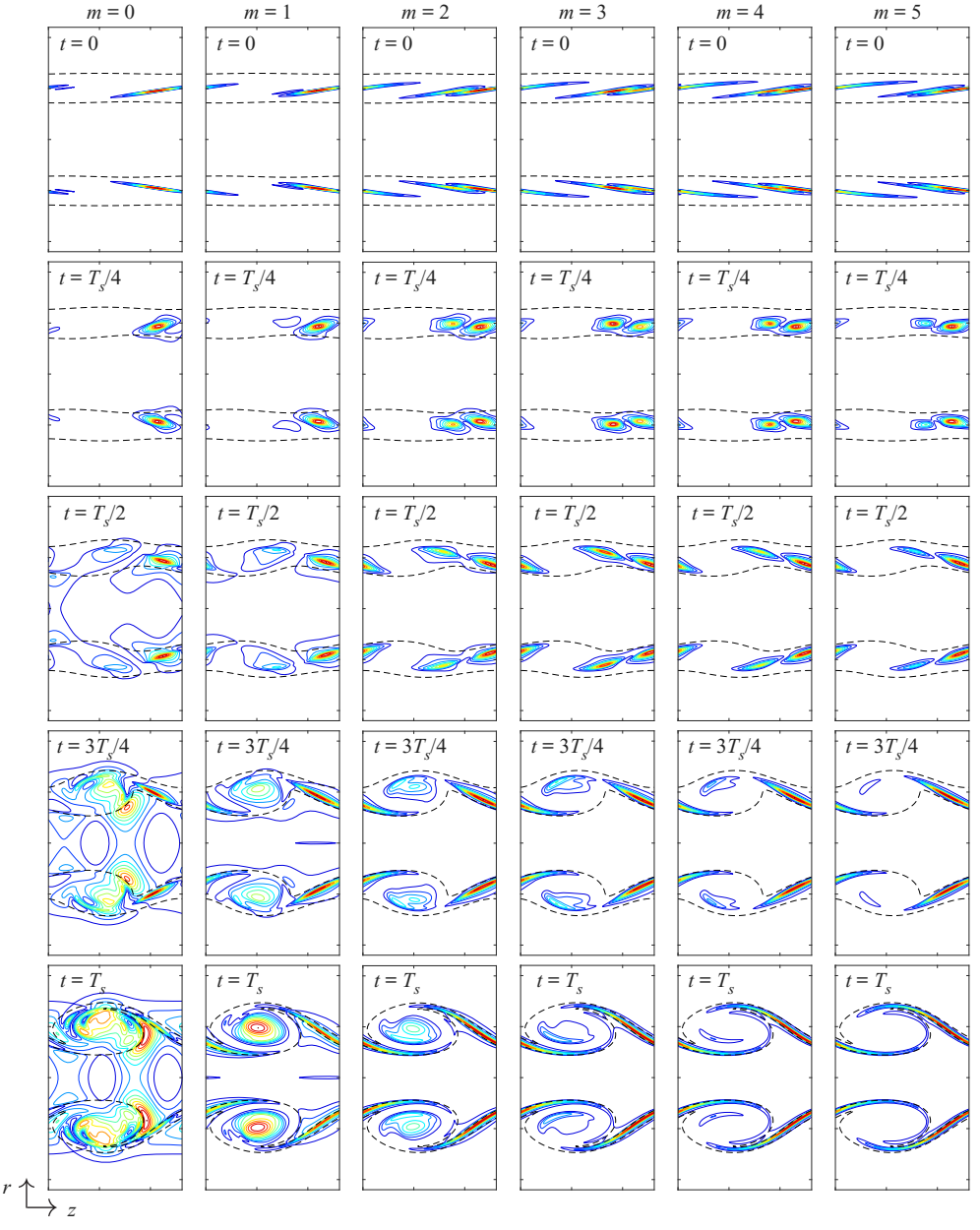

FIGURE 9. Temporal evolution of the field of kinetic energy E of optimal perturbations for $Re = 10\,000$ from $t = t_0$ to $t = T = T_s$ for various azimuthal wavenumbers. Same conventions as in figure 5.

normalised horizon time T/T_s obtained up to $T = 3T_s$ for the same values of azimuthal wavenumber as in the previous subsections. The optimal energy gain of perturbations growing over a diffusing unperturbed parallel jet has also been added in the background for reference. All amplification curves follow the same trend at the beginning, although perturbations characterised by higher azimuthal wavenumbers m present initial energy

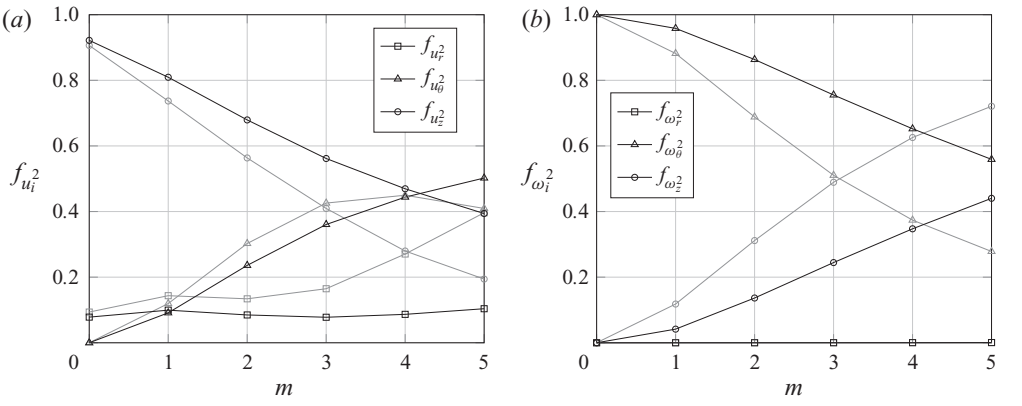

FIGURE 10. Initial contribution to (*a*) the energy of each velocity component $f_{u_i^2}$ and (*b*) the enstrophy of each vorticity component $f_{\omega_i^2}$, as a function of the azimuthal wavenumber m for $Re = 10\,000$ (black lines) and $Re = 1000$ (grey lines). The horizon time for the optimisation is $T = 1.5T_s$.

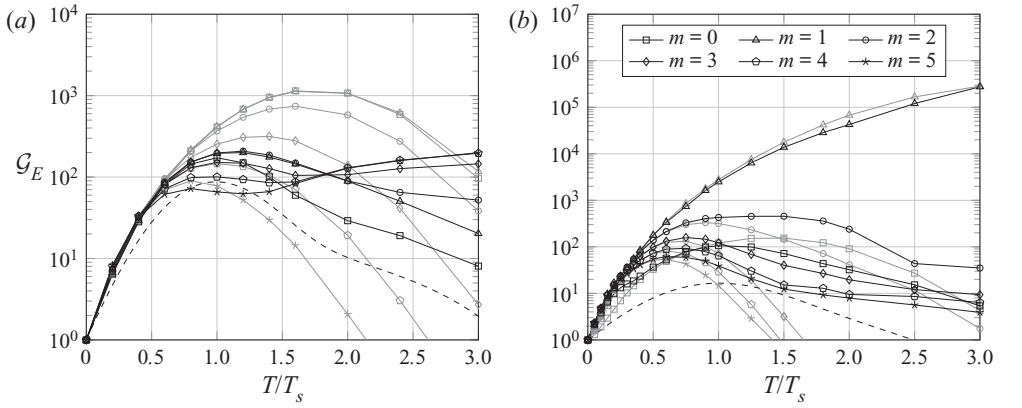

FIGURE 11. Optimal energy gain $\mathcal{G}_E$ as a function of the normalised horizon time T/T_s for different azimuthal wavenumbers at an injection time of $t_0 = 0$ for a base flow characterised by an aspect ratio of (*a*) $\alpha = 20$ and (*b*) $\alpha = 5$. Dashed black lines correspond to the temporal evolution of the energy gain G_E of the corresponding primary KH mode. Grey lines represent the optimal energy gain of perturbations growing over a diffusing Michalke profile.

growths slightly higher. As is the case with $\alpha = 10$, the essential part of the energy gain lies within the period of the linear evolution of the primary KH vortex ring during which the axisymmetric shear layer has not rolled-up yet. All disturbances developing during the unsteady base flow evolution towards the KH vortex ring feature a local maximum of the energy gain close to the saturation time T_s. For optimisation times larger than T_s, the energy gain decreases for $m \leq 2$ while it slightly increases for the other higher azimuthal wavenumber modes. The double-helix perturbation ($m = 2$) remains the global optimal until a little before twice the KH saturation time where it is superseded by an $m = 5$ disturbance. After such horizon time $T \approx 2T_s$, the flow would have bifurcated in the nonlinear regime to another state, so the helical and double-helix perturbations are

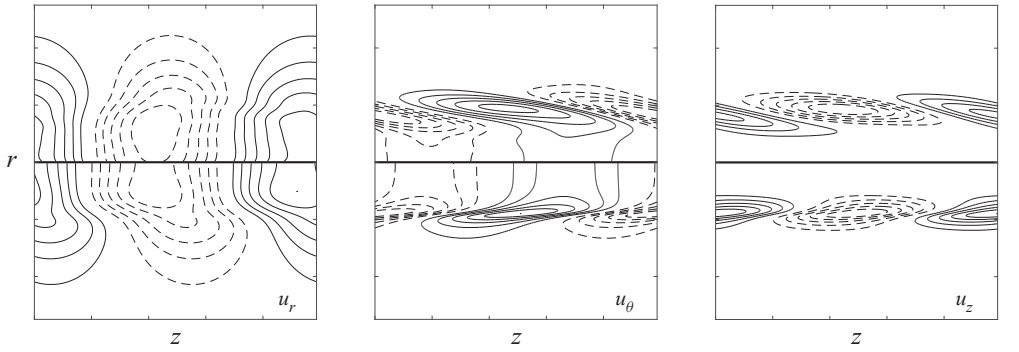

FIGURE 12. Contours of the velocity field of (upper half-plane) the optimal helical perturbation optimised for $T = 1.5T_s$ at a time of $t = 2T_s$ and (lower half-plane) the primary KH helical mode obtained by the linear stability analysis. In both cases, the initial jet profile has an aspect ratio of $\alpha = 5$. Contour levels are normalised by the maximal absolute value, solid (respectively, dashed) contours correspond to positive (respectively, negative) values. The thick continuous line in each panel represents the jet axis.

likely to be the ones growing in the round jet at $Re = 1000$. The increase in α associated with a scale reduction in shear layer momentum thickness ϑ promotes the emergence of a secondary mode of higher azimuthal periodicity, as is the case with the increase in Reynolds number.

Now we consider the optimal perturbations developing in a round jet characterised by a small aspect ratio, i.e. $\alpha = 5$. Unlike in the previous case with $\alpha = 20$, the axisymmetry condition has a strong influence on the evolution of the base flow which forms a low-aspect-ratio vortex ring. This case corresponds to the round jet behaviour where the large scale geometry and the curvature of the shear layer are expected to make some difference to the secondary behaviour of the plane shear layer. The final energy gain at horizon time as a function of the horizon time is given in figure 11(*b*) for wavenumbers up to 5, together with the final energy gain of perturbations growing over a diffusing Michalke profile. After an initial phase of energy growth with similar trends as for larger α, all perturbations see their energy decrease eventually with the horizon time. Only the helical perturbation exhibits a sustained energy growth with the horizon time. The $m = 1$ perturbation is the global optimal and reaches levels of energy gains three orders of magnitude larger than the others for $T = 3T_s$. It should be noted that, for this aspect ratio, the most unstable primary mode predicted by linear modal analysis is a helical KH mode (Jimenez-Gonzalez *et al.* 2015) and the primary axisymmetric KH mode considered here is not likely to arise naturally in the round jet, unless forced appropriately. Furthermore, its energy growth is practically superimposed on the one of the optimal perturbation growing over a diffusing Michalke profile, as shown in figure 11(*b*). This optimal perturbation for $m = 1$ taken at $t = 2T_s$ is thus compared with the primary KH helical mode given by the modal stability analysis of Michalke profile in figure 12. The optimal helical perturbation over a low-α round jet proves to be very similar to the helical KH modal instability of the jet. This is confirmed by the correlation coefficients between the two fields which are close to unity: 0.97 for the radial velocity component u_r, 0.94 for the azimuthal velocity component u_θ and 0.87 for the axial velocity component u_z. The axisymmetric KH vortex ring resulting from the KH instability in the base flow remains nested in the cylindrical shear layer during the nonlinear evolution of this low-Reynolds-number low-aspect-ratio

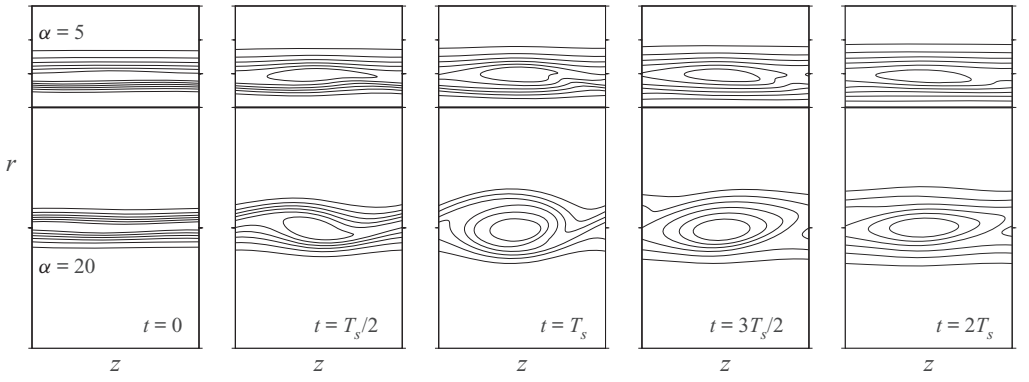

FIGURE 13. Temporal evolution of the azimuthal vorticity Ω_θ for a base flow corresponding to an aspect ratio of $\alpha = 5$ in the positive half-plane and $\alpha = 20$ in the negative half-plane. The azimuthal vorticity is normalised by its current time maximum value. Tick marks along the r axis correspond to the jet radius $\ell_0(\alpha)$ and the thick continuous line in each figure represents the jet axis.

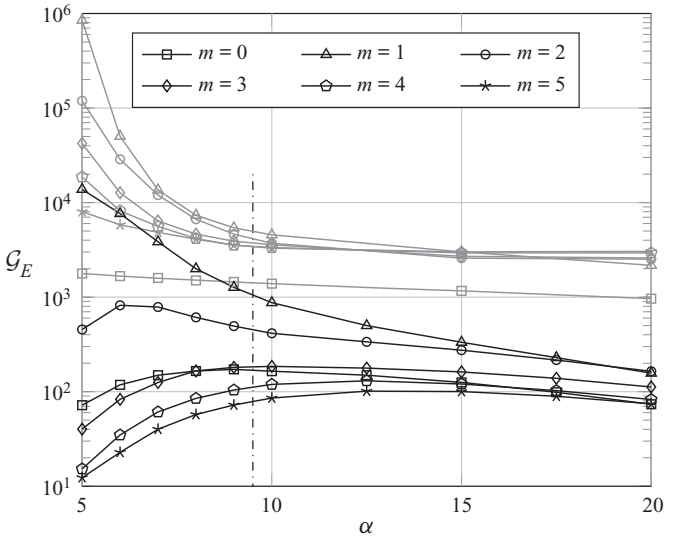

FIGURE 14. Optimal energy gain $\mathcal{G}_E$ in correspondence of a horizon time $T = 1.5T_s$ as a function of the aspect ratio α at $Re = 1000$ (black lines) and $Re = 10\,000$ (grey lines), for different azimuthal wavenumbers m. The dash-dotted line represents the value of aspect ratio $\alpha = 9.5$ below which the primary KH mode becomes helical.

jet. When compared with the $\alpha = 20$ case, as illustrated in figure 13, it appears that the overall structure of the $\alpha = 5$ base flow still resembles the one of the unperturbed jet. The small departure of this unsteady base flow from the parallel low aspect ratio one leaves it prone to transient and modal growth of helical perturbations, both in the first phase and in the long term.

This marked difference between the free shear layer and the pure round jet behaviours also emerges from figure 14 which presents the optimal energy gain $\mathcal{G}_E$ as a function of

the aspect ratio α obtained for a horizon time $T = 1.5T_s$, which stands as an intermediate horizon time in the nonlinear phase of the base flow. The influence of α is displayed for the same values of azimuthal wavenumbers m, together with the results obtained for $Re = 10\,000$. The dash-dotted line indicates the transition value of the aspect ratio, $\alpha = 9.5$, below which the most amplified primary KH mode over the Michalke profile is the helical one, while it is the axisymmetric one above. On the left of this threshold, the gain values at $1.5T_s$ are spread over a wide range with a strong predominance of the helical perturbation. For $Re = 1000$, the gain range between the helical perturbation and the less amplified one, i.e. $m = 5$, broadens up to three orders of magnitude for $\alpha = 5$. The same behaviour can be observed at $Re = 10\,000$, even though in this case the axisymmetric perturbation is the least amplified of all optimal perturbations for all values of α. On the other hand, the selection of the global optimal is less marked for higher aspect ratios $\alpha > 10$ with all the kinetic energy gains converging towards the same order of magnitude. The collapse of all final energy gain at $T = 1.5T_s$ on one threshold with increasing aspect ratio is even more pronounced at $Re = 10\,000$, with the sole exception of the axisymmetric perturbation ($m = 0$). Therefore, the increase of the aspect ratio is associated with a lower selectivity of the azimuthal periodicity of the global optimal. This can be related to the experimental observation of Liepmann & Gharib (1992) which found that, when the Reynolds number at the nozzle exit increases, i.e. when the shear layer thickness becomes thinner and α increases, the azimuthal wavenumber of secondary structures increases but the selection of the global optimal becomes weaker and less clear, as indicated by the error bars in their figure 15.

4. Conclusions

In this paper we have investigated numerically the transient linear growth of secondary three-dimensional perturbations in a time-evolving axisymmetric round jet subject to KH primary instability. The base flow is obtained from a nonlinear direct numerical simulation initialised with the velocity jet profile of Michalke (1971) perturbed by the primary axisymmetric KH mode determined by a classical modal stability analysis. A direct-adjoint technique is employed in order to identify the optimal perturbation maximising the gain of kinetic energy over a prescribed time interval $[t_0, T]$. We used two values of the Reynolds number, i.e. $Re = 1000$ and $Re = 10\,000$, and the aspect ratio α of the base flow has been varied in the range [5, 20].

For a base flow corresponding to an aspect ratio of $\alpha = 10$, the global optimal corresponds to a helical perturbation up to horizon times of $T \approx 2.5T_s$, beyond which the double-helix perturbation ($m = 2$) presents a slightly higher energy gain. At the injection time $t_0 = 0$, all the optimal perturbations can be properly described as 'OL' perturbations similar to those observed in plane shear layers by Arratia *et al.* (2013). They consist of two elongated oblique layers aligned along the direction of maximal compression of the base flow that are nearly similar regardless of the azimuthal wavenumber. They benefit from a synergy of both the Orr (1907) and the lift-up (Ellingsen & Palm 1975) mechanisms, going from pure Orr for $m = 0$ to a predominance of lift-up for $m = 5$. This results in an efficient transient energy growth within the initial period $[0, 0.5T_s]$ where the base flow is still quasi-parallel, a feature common to all azimuthal wavenumbers as indicated by the superimposition of all amplification curves. For larger horizon times, particularly after the KH saturation time T_s, the optimal perturbations evolve with increasing azimuthal wavenumber from an E-type perturbation centred in the core of the KH vortex ring to an H-type perturbation localised along the braid near the saddle point.

Increasing the Reynolds number yields larger energy gains for all perturbations without altering the physical mechanisms at play. The substantial rise of energy results from a higher base flow shear conversion due to the sharpening of KH roll-up velocity gradients combined with a diminution of the viscous dissipation. The effect on the spatial structure of the response is felt at high azimuthal wavenumber for which the energy is mostly, if not completely, concentrated in the braid region where the length scales of the base flow are much smaller.

Finally, we analysed the influence of the aspect ratio α which sets the influence of the axisymmetry condition on the base flow shear layer turning the round jet at low aspect ratios into a locally quasi-planar shear layer for large ones. In the latter case analysed for $\alpha = 20$, the cylindrical geometry does not bias the development of the perturbations which are very similar to those of a plane free shear layer. The history of energy growth remains similar to the case $\alpha = 10$ where the essential part of the energy gain is produced before the nonlinear roll-up of the primary KH wave into a vortex ring. The only difference lies in the selection of the azimuthal wavenumber of the global optimal for large horizon times. Indeed, the double-helix perturbation is the fastest growing until a little before twice the KH saturation time where it is superseded by the $m = 5$ disturbance. Therefore, increasing the aspect ratio also promotes the emergence of secondary modes with higher azimuthal periodicity. For as low aspect ratio as $\alpha = 5$, the base flow behaves as a pure round jet in which the influence of the cylindrical geometry is strong. The optimal energy gains exhibit an initial phase very similar to the one observed for large values of α, but beyond $T = 0.5T_s$ there is a clear separation of the gains for the different wavenumbers, and the optimal helical perturbation displays gains up to three orders of magnitude higher. The structure of the optimal perturbation proves to be very similar to the helical primary KH instability of the parallel round jet. In this case, the low-aspect-ratio base flow only slightly departs from the unperturbed parallel round jet which is more sensitive to the helical mode than to the axisymmetric one (Jimenez-Gonzalez *et al.* 2015).

It would be interesting, for future work, to perform a similar global stability analysis over a base flow where the primary KH instability is helical. The present approach could be extended to the variable-density case, as done by Lopez-Zazueta *et al.* (2016) for the plane shear layer, in order to investigate the features of the transient growth mechanism on mixing in light jets and their ability to trigger side ejections, as observed by Monkewitz *et al.* (1989, 1990). The work of Lopez-Zazueta *et al.* (2016) questioned the consensus on the underlying mechanism that has been proposed by Monkewitz & Pfizenmaier (1991) to explain side jets as the result of radial induction between pairs of counter-rotating longitudinal vortices. Instead, Lopez-Zazueta *et al.* (2016) proposed that side ejections result from the convergence of longitudinal velocity streaks near the braid saddle point. Carrying out the present non-modal stability approach on variable-density round jets will allow one to clarify this open question.

Acknowledgements

This research is supported in part by the French Ministry of Defence through financial support of the Direction Générale de l'Armement under grant number 2016635 and in part by the Institut Supérieur de l'Aéronautique et de l'Espace (ISAE-SUPAERO).

Declaration of interests

The authors report no conflict of interest.

Appendix A. The iterative optimisation algorithm

The outline of the iterative optimisation algorithm used to determine the optimal perturbation is given here (see Lopez-Zazueta 2015, for a comprehensive description).

(1) A white noise perturbation $\boldsymbol{q}^{(i)}(t_0)$ is chosen as an initial condition for the direct system (2.7). Its kinetic energy is given by

$$\|\boldsymbol{q}(t_0)\|_u = E_0, \tag{A 1}$$

where the seminorm

$$\|\boldsymbol{q}\|_u = \|\boldsymbol{u}\| = [\boldsymbol{q} \mid \boldsymbol{W}^u \cdot \boldsymbol{q}] \tag{A 2}$$

is associated with the inner product $[\star \mid \star]$ defined by

$$[\boldsymbol{q}_1 \mid \boldsymbol{q}_2] = \int_0^{r_{max}} \int_0^{2\pi} \int_0^{L_z} \boldsymbol{q}_1^* \cdot \boldsymbol{q}_2 r \, \mathrm{d}r \, \mathrm{d}\theta \, \mathrm{d}z + \text{c.c.}, \tag{A 3}$$

where the superscript * stands for the complex conjugate and the matrix operator $\boldsymbol{W}^u$ is defined by

$$\boldsymbol{W}^u = \begin{bmatrix} 1 & 0 \\ 0 & 0 \end{bmatrix}. \tag{A 4}$$

If any value for the constant E_0 is possible in practice, it was fixed here to $E_0 = 1$ for all cases.

(2) The direct system (2.7) is advanced in time from the injection time t_0 up to the horizon time T with the linearised version of the pseudo-spectral method used for the simulation of the primary KH vortex ring.

(3) The energy gain $G_E^{(i)}$ of the direct perturbation is calculated as defined by (2.9). Then, if the kinetic energy criterion

$$\frac{G_E^{(i)} - G_E^{(i-1)}}{G_E^{(i-1)}} \leq \varepsilon \tag{A 5}$$

is below a chosen threshold, here $\varepsilon = 0.005$, the iterative method has converged towards the optimal perturbation. Otherwise, we turn to the next step.

(4) The final state of the perturbation $\boldsymbol{q}(T)$ is used to compute the initial condition for the adjoint system (2.13) as follows:

$$\boldsymbol{W}^u \cdot \boldsymbol{q}^\dagger(T) = \boldsymbol{W}^u \cdot \boldsymbol{q}(T). \tag{A 6}$$

(5) The adjoint system (2.13) is integrated backward in time from T to t_0 with the same numerical pseudo-spectral method used for the direct equations.

(6) At the injection time t_0, the new initial condition $\boldsymbol{q}^{(i+1)}(t_0)$ is obtained through the optimality condition

$$\Lambda_u \boldsymbol{W}^u \cdot \boldsymbol{q}(t_0) - \boldsymbol{q}^\dagger(t_0) = 0, \tag{A 7}$$

where the Lagrange multiplier Λ_u is chosen so as to rescale the velocity field with respect to (A 1). Then we go back to step (2) until the convergence is reached.

REFERENCES

ABID, M., HUERRE, P. & BRACHET, M. 1993 Linear hydrodynamic instability of circular jets with thin shear layers. *Eur. J. Mech.* B/*Fluids* **12** (5), 683–693.

ARRATIA, C., CAULFIELD, C. P. & CHOMAZ, J.-M. 2013 Transient perturbation growth in time-dependent mixing layers. *J. Fluid Mech.* **717**, 90–133.

BATCHELOR, G. K. & GILL, A. E. 1962 Analysis of the stability of axisymmetric jets. *J. Fluid Mech.* **14** (4), 529–551.

BECKER, H. A. & MASSARO, T. A. 1968 Vortex evolution in a round jet. *J. Fluid Mech.* **31** (3), 435–448.

BORONIN, S. A., HEALEY, J. J. & SAZHIN, S. S. 2013 Non-modal stability of round viscous jets. *J. Fluid Mech.* **716**, 96–119.

BRANCHER, P., CHOMAZ, J.-M. & HUERRE, P. 1994 Direct numerical simulations of round jets: vortex induction and side jets. *Phys. Fluids* **6** (5), 1768–1774.

CAULFIELD, C. P. & KERSWELL, R. R. 2000 The nonlinear development of three-dimensional disturbances at hyperbolic stagnation points: a model of the braid region in mixing layers. *Phys. Fluids* **12** (5), 1032–1043.

CORBETT, P. & BOTTARO, A. 2000 Optimal perturbations for boundary layers subject to stream-wise pressure gradient. *Phys. Fluids* **12** (1), 120–130.

CORBETT, P. & BOTTARO, A. 2001 Optimal linear growth in swept boundary layers. *J. Fluid Mech.* **435**, 1–23.

CRIGHTON, D. G. & GASTER, M. 1976 Stability of slowly diverging jet flow. *J. Fluid Mech.* **77** (2), 397–413.

DRAZIN, P. G. & REID, W. H. 1981 *Hydrodynamic stability*. Cambridge University Press.

ELLINGSEN, T. & PALM, E. 1975 Stability of linear flow. *Phys. Fluids* **18** (4), 487–488.

FARRELL, B. F. 1988 Optimal excitation of perturbations in viscous shear flow. *Phys. Fluids* **31** (8), 2093–2102.

FARRELL, B. F. & IOANNOU, P. J. 1993 Perturbation growth in shear flow exhibits universality. *Phys. Fluids* A **5** (9), 2298–2300.

FONTANE, J. & JOLY, L. 2008 The stability of the variable-density Kelvin–Helmholtz billow. *J. Fluid Mech.* **612**, 237–260.

GARNAUD, X., LESSHAFFT, L., SCHMID, P. J. & HUERRE, P. 2013*a* Modal and transient dynamics of jet flows. *Phys. Fluids* **25** (4), 044103.

GARNAUD, X., LESSHAFFT, L., SCHMID, P. J. & HUERRE, P. 2013*b* The preferred mode of incompressible jets: linear frequency response analysis. *J. Fluid Mech.* **716**, 189–202.

GUNZBURGER, M. 2002 *Perspectives in Flow Control and Optimization*. Society for Industrial and Applied Mathematics.

JIMENEZ-GONZALEZ, J. I. & BRANCHER, P. 2017 Transient energy growth of optimal streaks in parallel round jets. *Phys. Fluids* **29** (11), 114101.

JIMENEZ-GONZALEZ, J. I., BRANCHER, P. & MARTINEZ-BAZAN, C. 2015 Modal and non-modal evolution of perturbations for parallel round jets. *Phys. Fluids* **27** (4), 044105.

JOLY, L., FONTANE, J. & CHASSAING, P. 2005 The Rayleigh–Taylor instability of two-dimensional high-density vortices. *J. Fluid Mech.* **537**, 415–431.

JOLY, L. & REINAUD, J. N. 2007 The merger of two-dimensional radially stratified high-Froude-number vortices. *J. Fluid Mech.* **582**, 133–151.

KHORRAMI, M. R., MALIK, M. R. & ASH, R. L. 1989 Application of spectral collocation techniques to the stability of swirling flows. *J. Comput. Phys.* **81** (1), 206–229.

KLAASSEN, G. P. & PELTIER, W. R. 1991 The influence of stratification on secondary instability in free shear layers. *J. Fluid Mech.* **227**, 71–106.

LANDAHL, M. T. 1975 Wave breakdown and turbulence. *SIAM J. Appl. Maths* **28** (4), 735–756.

LANDAHL, M. T. 1980 A note on an algebraic instability of inviscid parallel shear flows. *J. Fluid Mech.* **98** (2), 243–251.

LASHERAS, J. C., CHO, J. S. & MAXWORTHY, T. 1986 On the origin and evolution of streamwise vortical structures in a plane, free shear layer. *J. Fluid Mech.* **172**, 231–258.

LASHERAS, J. C. & CHOI, H. 1988 Three-dimensional instability of a plane free shear layer: an experimental study of the formation and evolution of streamwise vortices. *J. Fluid Mech.* **189**, 53–86.

LESSEN, M. P. & SINGH, P. J. 1973 The stability of axisymmetric free shear layers. *J. Fluid Mech.* **60** (3), 433–457.

LIEPMANN, D. 1991 Streamwise vorticity and entrainment in the near field of a round jet. *Phys. Fluids* A **3** (5), 1179–1185.

LIEPMANN, D. & GHARIB, M. 1992 The role of streamwise vorticity in the near-field entrainment of round jets. *J. Fluid Mech.* **245**, 643–668.

LOPEZ-ZAZUETA, A. 2015 Stabilité secondaire non-modale d'une couche de mélange inhomogène. PhD thesis, Université de Toulouse, Institut Supérieur de l'Aéronautique et de l'Espace.

LOPEZ-ZAZUETA, A., FONTANE, J. & JOLY, L. 2016 Optimal perturbations in time-dependent variable-density Kelvin–Helmholtz billows. *J. Fluid Mech.* **803**, 466–501.

LUCHINI, P. & BOTTARO, A. 1998 Görtler vortices: a backward-in-time approach to the receptivity problem. *J. Fluid Mech.* **363**, 1–23.

MARTIN, J. E. & MEIBURG, E. 1991 Numerical investigation of three-dimensionally evolving jets subject to axisymmetric and azimuthal perturbations. *J. Fluid Mech.* **230**, 271–318.

MICHALKE, A. 1964 On the inviscid instability of the hyperbolic-tangent velocity profile. *J. Fluid Mech.* **60** (4), 543–556.

MICHALKE, A. 1971 Instabilität eines kompressiblen runden freistrahls unter berücksichtigung des einflusses des strahlgrenzschichtdicke. *Z. Flugwiss* **8–9**, 319–328.

MICHALKE, A. 1984 Survey on jet instability theory. *Prog. Aerosp. Sci.* **21**, 159–199.

MONKEWITZ, P. A., BECHERT, D. W., BARSIKOW, B. & LEHMANN, B. 1990 Self-excited oscillations and mixing in a heated round jet. *J. Fluid Mech.* **213**, 611–639.

MONKEWITZ, P. A., LEHMANN, B., BARSIKOW, B. & BECHERT, D. W. 1989 The spreading of self-excited hot jets by side jets. *Phys. Fluids* **1** (3), 446–448.

MONKEWITZ, P. A. & PFIZENMAIER, E. 1991 Mixing by side jets in strongly forced and self-excited round jets. *Phys. Fluids* **3** (5), 1356–1361.

MORRIS, P. J. 1976 The spatial viscous instability of axisymmetric jets. *J. Fluid Mech.* **77** (3), 511–529.

MOSER, R. D. & ROGERS, M. M. 1993 The three-dimensional evolution of a plane mixing layer: pairing and transition to turbulence. *J. Fluid Mech.* **247**, 275–320.

ORR, W. M. F. 1907 The stability or instability of the steady motions of a perfect liquid and of a viscous liquid. Part I: A perfect liquid. Part II: A viscous liquid. *Proc. R Irish Acad.* A, **27**, 9–138.

ORTIZ, S. & CHOMAZ, J.-M. 2011 Transient growth of secondary instabilities in parallel wakes: anti lift-up mechanism and hyperbolic instability. *Phys. Fluids* **23** (11), 114106.

PIERREHUMBERT, R. T. & WIDNALL, S. E. 1982 The two-and three-dimensional instabilities of a spatially periodic shear layer. *J. Fluid Mech.* **114**, 59–82.

PLASCHKO, P. 1979 Helical instabilities of slowly divergent jets. *J. Fluid Mech.* **92**, 209–215.

REYNOLDS, W. C. & BOUCHARD, E. E. 1981 The effect of forcing on the mixing-layer region of a round jet. In *Unsteady Turbulent Shear Flows* (ed. R. Michel, J. Cousteix & R. Houdeville), pp. 402–411. IUTAM, Springer.

ROGERS, M. M. & MOSER, R. D. 1993 Spanwise scale selection in plane mixing layers. *J. Fluid Mech.* **247**, 321–337.

SCHMID, P. J. 2007 Nonmodal stability theory. *Annu. Rev. Fluid Mech.* **39** (1), 129–162.

YULE, A. J. 1978 Large-scale structure in the mixing layer of a round jet. *J. Fluid Mech.* **89** (3), 413–432.